Phospholipase D3 regulates lysosomal morphology, biogenesis, and function in neurons.

Yongchao Wang [1*], Cristian Carvajal-Tapia[1*], Stuti Jain[1], Emmeline Wang[1], Paige Rieschick[1], Nathaniel L. Hepowit[2], Nathan Appelbaum[1], Alex Prusky[1], Theodora Anghelina[1], Avelyn Kulsomphob[1], Vaibhav A. Janve[3,4], Samuel J. Frank[1], Alena Shostak[1], Timothy J. Hohman[3,4], Bret C. Mobley[5], Jason A. MacGurn[2], Wilber Romero-Fernandez[1†]and Matthew S. Schrag[1,3,5†]

[*]Equal contributions

[1]Department of Neurology, Vanderbilt University Medical Center, Nashville, Tennessee 37240, USA. Email: (Y.W) yongchao.wang@vumc.org, (C.C-T) cristian.o.carvajal@vumc.org, (S.J) jainstuti03@gmail.com, (P. R) paige.e.rieschick@vanderbilt.edu, (E.W) emmelinewang11@gmail.com, (N.A) nathaniappelbaum@gmail.com, (A.P) alexdprusky@gmail.com, (T.A) danghel001@gmail.com, (A.K) avelynkulsomphob@gmail.com, (S. J. F) samuel.j.frank.1@vanderbilt.edu, (A.S) alena.shostak@vumc.org, (W.R-F) wilber.romero.fernandez@vumc.org and (M.S.S) matthew.schrag@vumc.org

[2]Department of Cell and Developmental Biology, Vanderbilt University, Nashville, Tennessee 37240, USA. Email: (N.H) nat.hepowit@vanderbilt.edu, (J.A.M) jason.a.macgurn@vanderbilt.edu

[3] Vanderbilt Genetics Institute, Vanderbilt University Medical Center, Nashville, Tennessee 37232, USA. Email: (T.J.H) timothy.j.hohman@vumc.org, (V.A.J) vaibhav.a.janve@vumc.org.

[4]Vanderbilt Memory and Alzheimer's Center, Vanderbilt University, Nashville, Tennessee 37235, USA.

[5]Department of Pathology, Microbiology, and Immunology, Vanderbilt University Medical Center, Nashville, Tennessee, USA. Email: (B.C.M) bret.mobley@vumc.org

[†]*Corresponding authors:*

Department of Neurology, Vanderbilt University Medical Center
MRBIII 465 21st Avenue S, Suite 6158 Nashville, Tennessee 37232, USA
Matthew S. Schrag, M.D., Ph.D.
E-mail: matthew.schrag@vumc.org, Tel: +(1)615-936-0060
Wilber Romero-Fernandez, Ph.D.
E-mail: wilber.romero.fernandez@vumc.org, Tel: +(1) 615-7848784

Abstract

Phospholipase D3 (PLD3) is a lysosomal protein in neurons and is linked to an Alzheimer's disease (AD) risk through coding variants. Its role in lysosomal abnormalities observed in AD remains unclear. We conducted a comprehensive study integrating transcriptomic, proteomic, and cell biology approaches to investigate PLD3's role in lysosome function in neurons.

PLD3 undergoes aberrant ubiquitination in AD brain tissue, leading to altered protein abundance and subcellular location. We assessed the lysosomal proteome in SH-SY5Y cells with PLD3 knockout and found PLD3$^{-/-}$ cells had higher levels of proteins related to lysosomal biogenesis, endocytosis, and calcium signaling. Loss of PLD3 caused an enlargement in neuronal lysosome size, increased endocytic activity and a decline in lysosomal clearance of aggregated human β-amyloid or α-synuclein, despite increased expression level and activity of cathepsin B. PLD3-deficiency increase the level and transcriptional activity of transcription factor EB (TFEB) and transcription factor binding to IGHM enhancer 3 (TFE3), suggesting a role for PLD3 in regulating lysosomal biogenesis.

In summary, we found that PLD3 is required to maintain neuronal lysosomal function.

Keywords

Alzheimer's Disease; Phospholipase D3; Transcription factor EB; transcription factor binding to IGHM enhancer 3; Cathepsin B; Ubiquitin; Ubiquitination; Lysosome biogenesis.

Background

Alzheimer's disease (AD) is the most common cause of dementia. It is characterized by a broad range of neuropathologies, including extracellular accumulation of β-amyloid (Aβ) in plaques and cerebral vessels, intraneuronal tangles and neuropil threads composed of hyperphosphorylated tau, dystrophic neurites, granulovacuolar degenerating bodies, and synaptic loss (1, 2).

57 Degradation of waste proteins in neurons is managed by the concerted action of the ubiquitin-
58 proteasome (UPS) (3) and the endosome-autophagosome-lysosome pathways (EAL) (4). If these
59 clearance pathways are dysregulated, proteins may accumulate and impair cellular homeostasis.
60 Aberrant ubiquitination and dysfunction in UPS have long been associated with AD (5, 6).
61 Many studies have implicated sub-optimal function of lysosomal machinery in the pathogenesis of
62 neurodegenerative proteinopathies (7, 8). Various factors, including alterations in lysosome size,
63 population or trafficking, pH regulation, EAL disruption, and lysosomal membrane
64 permeabilization, can cause lysosomes to malfunction (9, 10). Lysosomal deacidification, which
65 could contribute to inefficient function of the more than 60 lysosomal hydrolases, has been
66 hypothesized to play a role in the pathogenesis of several neurodegenerative diseases (11, 12).
67 Lysosomal biogenesis is regulated by Transcription factor EB (TFEB) and transcription factor
68 binding to IGHM enhancer 3 (TFE3) levels and activity, because TFEB and TFE3 govern the
69 expression of a network of genes linked to lysosomal biogenesis and autophagy (13-16). Alterations
70 in the TFEB/TFE3 pathway have been observed in AD *(for a review, see (15))*. It has been reported
71 that genetic disruption of TFEB results in defective microglia activation and increased tau pathology
72 (17).
73 Restoring lysosomal homeostasis would likely be beneficial for treating AD, so understanding the
74 role of lysosomal proteins like PLD3, which is linked to AD risk, is a key priority.
75 PLD3 is a member of the phospholipase D family and is primarily localized to lysosomes. It is
76 highly expressed in neurons (18, 19). A growing body of evidence has linked PLD3 to AD (20, 21).
77 PLD3 is remarkably enriched in dystrophic neurites surrounding ß-amyloid plaques in AD(21).
78 Axonal PLD3 accumulation was functionally implicated in the formation and growth of dystrophic
79 neurites, contributing to neural network defects in AD (22). Lysosomes in neurons of PLD3

knockout mice exhibited significant enlargement (23). Despite its localization in neuronal lysosomes, its role(s) in lysosomal function remains a matter of ongoing study, with recent evidence pointing to a role in lysosomal degradation of lipids and nucleic acids (24, 25).

Our study presents evidence supporting a causal link between PLD3 and lysosome abnormalities occurring in AD, including morphological changes and impairment of degradative function that can promote proteostasis disturbance. Additionally, we demonstrate that PLD3 regulates TFEB/TFE3 signaling, suggesting a role in lysosomal biogenesis.

Methods

Human brain tissue.

Brain tissue was obtained from the Vanderbilt Brain and Biospecimen Bank at Vanderbilt University Medical Center, Nashville, Tennessee, USA (IRB# 180287). Written informed consent for each anatomical donation was obtained from patients or their surrogate decision-makers. The Vanderbilt University Medical Center Institutional Review Board provided ethical supervision, and the study was performed in accordance with the ethical principles of the Declaration of Helsinki.

Antibodies and reagents

Primary antibodies used in this study include: rabbit anti-PLD3 (HPA012800, Sigma-Aldrich, St. Louis, MO, 1:1000 for WB and 10 μg/mL for IHC), mouse anti-ubiquitin clone Ubi-1 (13-1600, Invitrogen, Carlsbad, CA, 1:1000 for WB and 10 μg/mL for IHC), mouse anti-TFEB (91767, Cell Signaling Technology, Boston, MA, 1:1000 for WB, 1:100 for IF), rabbit anti-TFE3 (81744, Cell Signaling Technology, 1:1000 for WB), mouse anti-Lamin B1 (66095, Proteintech, Rosemont, IL, 1:1000 for WB), mouse anti-LC3B (83506, Cell Signaling Technology, 1:1000 for WB), mouse anti-LAMP2 (H4B4, DSHB, Iowa, IA, 1:1000 for WB and 10 μg/mL for IHC), mouse anti-GAPDH (ab59164, Abcam, Cambridge, UK, 1:5000 for WB), mouse anti-GAPDH (60004-1-Ig; Proteintech,

103 1:1000 for WB), mouse anti-GAPDH-HRP (60004; Proteintech, 1:1000 for WB), rabbit anti-β-
104 Tubulin (15115, Cell Signaling Technology, 1:5000 for WB), goat anti-CTSB (AF965, R&D
105 Systems, Minneapolis, MN, 1:1000 for WB and 10 μg/mL for IHC), goat anti-CTSD (AF1014,
106 R&D systems, 1:1000 for WB and 10 μg/mL for IHC), rabbit anti-IKKβ (8943, Cell Signaling
107 Technology, 1:1000 for WB), normal rabbit IgG (12-370, Cell Signaling Technology).
108 Secondary antibodies used in this study include: goat anti-mouse IgG (H+L), HRP (62-6520;
109 Invitrogen), goat anti-rabbit IgG (H+L), HRP (65-6120; Invitrogen), IRDye® 800 CW goat anti-
110 rabbit (926-32211; LI-COR, Lincoln, NE), IRDye® 680 RD goat anti-mouse (926-68070; LI-COR),
111 IRDye® 680 LT donkey anti-goat (926-68024; LI-COR), IRDye® 800 CW donkey anti-rabbit
112 (926-32213; LI-COR), and IRDye® 800 CW donkey anti-mouse (926-32213; LI-COR).
113 Reagents used in this study include: synthetic human β-amyloid$_{1-42}$ (AG968; Sigma-Aldrich), DQ
114 Green BSA (D12050, ThermoFisher Scientific), dextran Oregon Green 488 (D7172, ThermoFisher
115 Scientific), Protein G/A agarose supernatant (IP05, Millipore, Burlington, MA), dextran Alexa
116 Fluor 594 (D22913, ThermoFisher Scientific), dextran Alexa Fluor 647 (D22914, ThermoFisher
117 Scientific), Alexa Fluor 647 BSA (A34785, ThermoFisher Scientific), CellLight Lysosome-RFP
118 BacMam 2.0 (C10597, ThermoFisher Scientific), Torin 1 (14379, Cell Signaling Technology),
119 Hoechst 33342 (R37605, ThermoFisher Scientific, two drops/ml), neurobasal-A medium, minus
120 phenol red (12349015, ThermoFisher Scientific), 1 μM 4,4'-[(2-methoxy-1,4-phenylene) di-(1*E*)-
121 2,1-ethenediyl] bisphenol (MX-04) (Tocris, Minneapolis, MN), Thiazine Red (1 μM, Chemsavers
122 Inc, Bluefield, VA), 4 ', 6-diamidino-2-phenylindol (1 μM, DAPI, Cayman Chemical, Ann Arbor,
123 MI), TO-PRO™-3 (1 μM, ThermoFisher Scientific). Potent and specific CTSB inhibitor CA074 (1
124 μM, 4863, Tocris). The information for all other reagents is indicated in the corresponding sections.
125 Details of specific methods are provided in the supplementary material.

126 *Brain tissue preparation, immunostaining, and proximity ligation assay.*

127 Human brain tissue was prepared as previously described (26). Immunohistochemical labeling was
128 performed as described (21, 26-28). PLD3-ubiquitin complex detection in postmortem human brain
129 was performed using the Duolink® Proximity Ligation Assay (PLA) kit (Sigma-Aldrich), following
130 the protocol previously described (29, 30), including modifications optimized for a fluorescent
131 format in the human brain (26).

132 *Human Aβ seeds extraction.*

133 Human Aβ seeds were isolated as previously described (31) with minor modifications. Seeds were
134 isolated from the brain tissue of patients with severe cerebral amyloid angiopathy (CAA) with
135 minimal other neuropathology. Briefly, tissue was homogenized, and the lipid-rich fraction was
136 removed by centrifuging in 17% dextran (40,000 MW, Sigma-Aldrich) at 10,000 x g for 5 minutes.
137 The pellet was resuspended in TBS (Corning, Corning, NY), and the suspension was filtered
138 through a custom-designed 3D printed microsieve apparatus with 40 µM pore size to isolate
139 microvascular fragments. Aggregates of β-amyloid were freed from the vascular matrix by
140 incubating with 3 mg/ml Collagenase Type I (Gibco, Billings, MT) overnight at 37°C and gently
141 homogenizing with 12 passes of a Dounce homogenizer. The suspension was again passed through
142 the microsieve, and the liquid containing the particles was centrifuged and resuspended in TBS
143 (Corning). It was pelleted and resuspended twice more to remove any residual enzyme. The
144 particles were disrupted with sonication to produce a microparticulate suspension with a mean
145 particle diameter of around 10 microns (particle size distribution shown in Fig. S7). Before adding
146 to cells, particles were further disrupted with sonication to produce a microparticulate suspension
147 with a mean particle diameter of about 1 micron (Fig. S7).

148 *PLD3 knockout cell line*

149 SH-SY5Y cell line (CRL-2266, ATCC) was used to generate PLD3 knockout (SH-SY5Y PLD3$^{-/-}$),
150 performed by Abcam (Abcam, Waltham, MA). PLD3-g1: AGCCCACAACCGCCAGAATG and
151 PLD3-g2: TACTCGCAAGGGTCATAGCA were transfected into SH-SY5Y cells individually with
152 the Cas9 gene to generate the PLD3 knockout two PLD3 knockout clone 3 (PLD3$^{-/-}$) and clone 14
153 PLD3$^{-/-c14}$). A DNA deletion (~100 bp) in exon 5 of the PLD3 gene in both alleles was achieved,
154 making the frameshift knockout. PCR subsequently confirmed the resulting DNA deletion and was
155 further validated at the protein level by western blotting. Unless otherwise specified, all experiments
156 were performed with clone 3 (PLD3$^{-/-}$).
157 *Cell culture, cDNA transfection, siRNA, differentiation to neurons, and drug incubation.*
158 SH-SY5Y wild type (WT, CRL 2266, ATCC) and SH-SY5Y PLD3$^{-/-}$ cells were grown in
159 DMEM/F12 (Gibco) supplemented with 10% (v/v) fetal bovine serum (FBS, Corning) and 100
160 μg/mL Normocin (InvivoGen) or 1% penicillin/streptomycin (0503, ScienceCell, Carlsbad, CA) at
161 37°C in a humidified atmosphere of 5% CO_2.
162 PLD3 plasmids were from Sino Biological (Beijing, China), and the PLD3 mutant plasmids were
163 previously generated using a site-directed mutagenesis kit (21). GFP-N-TFEB (38119, Addgene)
164 and its corresponding control (60360, Addgene) plasmids were from Addgene. PLD3 siRNAs and
165 their corresponding control siRNAs were purchased from IDT. For plasmid transfection, plasmid
166 DNA was transfected into cells with Lipofectamine 3000 reagent following the manufacturer's
167 protocol (L3000015, Invitrogen). For siRNA transfection, cells were transfected with 10 μM siRNA
168 by Oligofectamine™ reagent per the manufacturer's recommendations (12252-011, Invitrogen).
169 SH-SY5Y differentiation into neurons was performed as previously described (32).
170 Cells were incubated with and without synthetic β-amyloid$_{1-42}$ (1 μg/mL) for 1, 3, 5, or 7 days
171 before treatment with DMSO, dextran (0.25 mg/mL), HBSS, or Torin 1 (1 μM) for 3 hours at 37°C,

172 followed by washing with PBS for 10 minutes. The cells were then fixed following
173 immunocytochemistry as described above. Subcellular fluorescence was detected, imaged, and
174 analyzed using the CellInsight CX7 LED Pro HCS Platform.
175 *Human induced pluripotent stem cell (iPSC) maintenance and differentiation to neurons.*
176 CC3 iPSCs (33) were maintained and differentiated into cortical glutamatergic neurons as
177 previously described (34) with minor modifications (35). iPSC neurons in culture were incubated
178 with and without human β-amyloid seeds (100 ng/mL) for 2, 3, 5, or 7 days before performing
179 protein extraction, SDS-PAGE, and western blot as described below, or immunocytochemistry as
180 described above.
181 *Cathepsin B activity measurement.*
182 Cells were plated at a concentration of $5 \times 10^{\wedge 6}$ cells/75 cm^2 flasks and cultured overnight before
183 assay. Cells were collected, and the CTSB enzymatic activity was measured according to the
184 guidelines of SensoLyte® 520 Cathepsin B Assay Kit Fluorometric (AS-72164; AnaSpec, Fremont,
185 CA). Results were normalized to the total protein concentration determined by Pierce™ BCA
186 Protein Assay Kit (23225; ThermoFisher Scientific) and enzymatic activity in the presence of the
187 potent and selective inhibitor of CTSB, CA074 (1 μM).
188 *Protein extraction, SDS-PAGE, and western blot.*
189 Cell protein homogenates, and grey matter, and white matter tissue lysates were prepared as
190 described previously (21). SDS-PAGE and western blot were performed as described previously
191 (21).
192 *Lysosome labeling with dextran.*
193 Cells were seeded at a concentration of $40 \times 10^{\wedge 3}$ cells per well in Nunc microwell 96-well optical-
194 bottom plates and allowed to attach overnight. The cells were then incubated with dextran Oregon

195 Green (0.25 mg/mL) and dextran AlexaFluor 594 (0.25 mg/mL) overnight at 37°C, followed by a
196 chasing period of 6 hours to minimize endosome labeling. The staining medium was removed, and
197 the cells were incubated with Neurobasal medium containing Hoechst for 2 hours at 37°C. The
198 subcellular fluorescence patterns were quantified using CellInsight CX7 and the LED Pro HCS
199 Platform.

200 *Co-localization analysis of dextran and LAMP1-RFP.*

201 Cells were seeded at 40 × 10^3 cells per well in Nunc microwell 96-well optical-bottom plates and
202 allowed to attach overnight. A construct expressing LAMP1-fused RFP was delivered into cells
203 using BacMam 2.0 technology to target lysosomes. On the second day, the medium was removed,
204 and the cells were incubated with dextran AlexaFluor 647 (0.25 mg/mL) overnight in the incubator,
205 followed by a chasing period of 6 hours. The staining medium was removed, and the cells were
206 stained with Hoechst in neurobasal-A medium with clear color for 2 hours at 37°C. The subcellular
207 fluorescence patterns were quantified using CellInsight CX7 and the LED Pro HCS Platform.

208 *Lysosomal function assay.*

209 Cells were seeded at 40 × 10^3 cells per well in Nunc microwell 96-well optical-bottom plates and
210 allowed to attach overnight. The cells were then treated with DMSO, Torin-1 (1 μM), or
211 Bafilomycin A (100 nM) for 3 hours, followed by incubation with DQ Green BSA (10 μg/mL) and
212 Alexa Fluor 647 BSA (10 μg/mL) for 3 hours. The assay medium was removed, and the cells were
213 incubated with Hoechst in neurobasal-A medium for nuclear staining for 2 hours at 37°C.
214 Subcellular fluorescence was subsequently analyzed using the CellInsight CX7 LED Pro HCS
215 Platform.

216 *Spot detection and quantification by CellInsight CX7 LED Pro HCS platform.*

217 Subcellular fluorescence was detected and imaged in acquisition mode on the CX7 HCS platform.
218 Images *(n=30-50)* per well were automatically captured using laser autofocus, and the in-focus
219 pictures were selected for subsequent analysis. For quantification analysis, images were first
220 preprocessed with background removal, smoothing, and segmentation, followed by spot (fluorescent
221 signals) identification and validation. The spots were compartmentalized into the cell body part
222 (circle) and the distal part (ring). All images were re-scanned in disk mode, and the information
223 about spot area and intensity (total and average) on all channels was reported and statistically
224 analyzed. Three to six independent experiments *(n=3-6)* were performed for final statistical
225 analysis.
226 *Transmission electron microscopy.*
227 Cells were fixed in 0.1 M cacodylate buffer containing 2.5% glutaraldehyde, harvested using a cell
228 scraper, and pelleted. Samples were then sequentially postfixed in 1% tannic acid and 1% OsO4,
229 followed by en block staining in 2% uranyl acetate. After post-fixation, the samples were
230 dehydrated in a graded ethanol series and infiltrated with Quetol 651-based Spurr's resin using
231 propylene oxide as a transition solvent. The resin was polymerized at 60 °C for 48 hours, and 70 nm
232 sections were cut on a Leica UC7 ultramicrotome.
233 Imaging was performed on a JEOL 2100+ transmission electron microscope operating at 200 keV,
234 with images captured using an AMT nanosprint CMOS camera. Single images were acquired with
235 AMT imaging software, while tiled image sets were acquired using SerialEM automation software.
236 Tiled datasets were processed using the IMOD/etomo software suite and FIJI. Lysosome
237 characteristics were analyzed and quantified using FIJI.
238 *Lysosomal protein preparation.*
239 Lysosomes were isolated and purified as described previously (21).

240 *Isolation of cytoplasmic and nuclear proteins.*

241 Cytoplasmic *(c)* and nuclear *(n)* proteins were isolated from cells of interest following the
242 instructions in the manufacturer's user guide (78833, ThermoFisher Scientific).

243 *Mass spectrometry and bioinformatic analysis.*

244 Protein samples were prepared with 5% SDS, processed using S-Trap (ProtiFi) digestion, and
245 analyzed by LC-MS/MS, following a protocol described previously (36). The LC-MS/MS data were
246 analyzed using MaxQuant against a human database created from the UniprotKB protein database,
247 with MaxQuant contaminants added (37). Standard MaxQuant parameters were applied, along with
248 LFQ and match-between-runs. Variable modifications included methionine oxidation and N-
249 terminal acetylation, while carbamidomethyl cysteine was a fixed modification. A false discovery
250 rate (FDR) 0.01 was applied to peptide and protein identifications. Label-free quantitative (LFQ)
251 analysis of the identified proteins was performed using the MSstats R package with default
252 parameters (38).

253 *RNA extraction, sequencing, and bioinformatic analysis.*

254 Total RNA was isolated from cells of interest using RNeasy Mini Plus Kits (74134, Qiagen)
255 following the manufacturer's protocol, with each group having three replicates. RNA quality control
256 was performed using the Agilent Bioanalyzer, and RNA quantity was determined using the RNA
257 Qubit assay (Q10210, ThermoFisher Scientific).

258 *Library preparation and RNA sequencing.*

259 Library preparation was started with ribosomal RNA removal using the NEBNext® rRNA
260 Depletion kit and 500 ng of input total RNA (E6310L, New England Biolabs). Following rRNA
261 depletion, the RNA samples were subjected to mRNA enrichment using oligo(dT) beads, and
262 subsequent fragmentation was done using divalent cations at an elevated temperature. Libraries

263 were generated by cDNA synthesis with random hexamer primers, RNase H digestion, A-tailing,
264 and adapter ligation. The cDNA libraries were assessed for quality with a Bioanalyzer and
265 quantified using the KAPA Library Quantification Kit according to the manufacturer's
266 recommendations (KK4824, Roche). The libraries were mixed in equal molar ratios, and the
267 resulting library pools underwent cluster generation using the NovaSeq 6000 System according to
268 the manufacturer's protocol. A 150 bp paired-end sequencing was performed on the NovaSeq 6000
269 platform, which was set to target 30M reads per sample. Real-Time Analysis Software (RTA) and
270 NovaSeq Control Software (NCS) (1.8.0; Illumina) were used for base calling. MultiQC (v1.7;
271 Illumina) was used for data quality assessments.

272 *Bioinformatic analysis.*

273 The raw sequencing data (FASTQ files) were subjected to quality and adapter trimming and quality
274 control using the wrapper program, Trim Galore. The GRCh38 human transcriptome from
275 GENCODE was used to build the transcriptome index with the Kallisto program (39). After being
276 processed by Trim Galore, the sequences were mapped and quantified into transcript-level
277 abundance using the Kallisto program (39). Transcript-level abundance was then summarized into
278 gene-level abundance, followed by differential gene expression analysis using DESeq2 in R (40).
279 Heatmap representation of gene-level abundance, principal component analysis (PCA), and volcano
280 plot representation of differentially expressed (DE) genes were all performed and graphed with R.
281 Normalized RNA-Seq quantification was then submitted to the GSEA website for gene set
282 enrichment analysis (GSEA) with c2.cp.kegg_legacy.v2023.2.Hs.symbols.gmt as the gene set
283 database (41).

284 *Statistical analyses*

285 The number of samples (*n*) in each group/experimental condition is indicated in the figure legends.
286 All data were graphed and statistically analyzed using GraphPad software (version 10.0.2,
287 GraphPad Software Inc., San Diego, CA) or R packages unless stated otherwise. For gene set
288 enrichment analysis, statistical tests were based on the Kolmogorov-Smirnov test (41). For RNA-
289 Seq differential gene expression analysis, the data were subject to negative binomial generalized
290 linear model fitting and Wald statistics (40). The parametric unpaired *t*-test or the Welch's unequal
291 variances *t*-test was used to compare two groups. Ordinary one-way ANOVA was used to compare
292 more than two independent groups, followed by Tukey's, Dunnett multiple comparisons, or
293 Uncorrected Fisher's LSD. Non-parametric Kruskal-Wallis tests were performed, followed by
294 Dunn's multiple comparisons test. Two-way ANOVA tests were performed to assess the individual
295 and interaction effects of two variables, followed by the Dunnett test. Statistical tests were specified
296 and noted in the respective figure legends. Unless stated otherwise, a significant level of 0.05 was
297 used to reject the null hypothesis throughout this article.

298 **Results**

299 **PLD3 is a target of aberrant ubiquitination in human brain with AD resulting in its altered**
300 **subcellular location.**

301 Immunohistochemistry with a validated antibody (Fig. S1) in brain sections without AD (Braak
302 I-II) showed high immunoreactivity for PLD3 in a punctate pattern in all regions analyzed (Fig.
303 1A and Fig. S2), consistent with the expected lysosomal subcellular distribution. In sections from
304 patients with AD (Braak III-VI), PLD3 was less abundant in healthy-appearing neurons and was
305 enriched in dystrophic neurites surrounding β-amyloid plaques and in neuropil threads and
306 neurofibrillary tangles (Fig. 1B and Fig. S2).

307 PLD3 was observed mainly in grey matter and was sparse in white matter (Fig. S3A). In non-AD
308 grey matter, the PLD3 signal colocalized primarily with a neuronal marker (Fig. S3B-C) and
309 occasionally with a microglia marker (Fig. S3D), but not with a marker for astrocytes (Fig. S3E).
310 PLD3 was present in white matter, with more frequent co-localization with a microglia marker,
311 but PLD3 level in AD white matter was not significantly different compared to non-AD white
312 matter (Fig. S3F-G).
313 We evaluated the PLD3 levels by western blot in grey matter (Fig. 1C and Fig. S4A) and white
314 matter (Fig. 1D and Fig. S4B) in homogenates of human temporal lobe tissue. We observed
315 additional bands to the previously reported primary 50 and 70 kDa bands (42). These additional
316 bands could be products of posttranslational modifications and were included in the total PLD3
317 quantification as they appeared to be specific in our verification experiments (Fig. S1). In grey
318 matter, there was approximately a 38% reduction in total PLD3 levels in AD (Fig. 1C and Fig.
319 S4A). No significant differences in total, lumenal, and membrane-associated PLD3 levels were
320 found in white matter (Fig. 1D and Fig. S4B).
321 An initial report that PLD3 may regulate β-amyloid and/or APP levels was not reproducible in
322 our work (21) and the work of others (23). Still, it remains unclear whether PLD3 levels are
323 affected by β-amyloid. We evaluated the effect of a 7-day exposure of synthetic $A\beta_{1-42}$ (1 μg/mL)
324 on PLD3 levels in a human neuroblastoma cell line (SH-SY5Y cells, Fig. 1E and Fig. S5A). We
325 detected a significant decrease in PLD3 on the third day but not in the following days (Fig. 1E).
326 A substantial reduction in PLD3 level was found in analogous experiments using iPSC-derived
327 neurons *(a cell line from a neurologically normal, young female donor)* incubated with brain-
328 derived β-amyloid seeds from patients with cerebral amyloid angiopathy (CAA) (100 ng/mL)

329 (Fig S5B-D). This decrease persisted after the third day (Fig. 1F and Fig. S5E). The average
330 lysosomal size was increased after exposure to brain-derived β-amyloid seeds Fig. S6.
331 The decreased level of PLD3 in the brain is partly due to reduced transcription (43). Still,
332 ubiquitination could contribute to accelerated degradation and/or altered localization within the
333 brain, as was suggested in previous cell-culture based experiments (42). For this reason, we
334 sought to visualize ubiquitinated PLD3 in human brain tissue. Ubiquitin immunochemistry
335 revealed the marked accumulation of ubiquitin which is expected in AD brains (Fig. S7A-B). *In-*
336 *situ* PLA confirmed proximity between PLD3 and ubiquitin, consistent with ubiquitin
337 modification of PLD3 (Fig. 1G and Fig. S8C). In non-AD brain sections, PLA puncta
338 corresponding to PLD3-ubiquitin complexes were sparse (Fig. 1G, *right panel*), while
339 significantly greater levels of PLA puncta were observed in AD brain sections (Fig. 1G, *left*
340 *panel*). PLD3-ubiquitin complexes were partially localized to tau pathology (Fig. 1G, *left panel*,
341 and Fig. S8C). There was a 4.8-fold increase in the number of PLA puncta/field in AD compared
342 to non-AD (Fig. 1G). We found scarce PLA puncta in technical and biological controls for *in-*
343 *situ* PLA (Fig. S8D).
344 We combined *in-situ* PLA with IHC to visualize the subcellular location of PLD3-ubiquitin
345 complexes. In both non-AD and AD brain sections, PLD3-ubiquitin complexes were negatively
346 correlated with lysosome staining as shown by CTSD immunostaining ($p = 0.3149$ by unpaired
347 *t*-test with Welch's correction, Fig. 1H), suggesting the lysosomal localization of PLD3 is lost
348 when it is ubiquitinated.
349
350 **Loss of PLD3 alters lysosome morphology and function and remodels the lysosomal**
351 **proteome.**

352 We obtained and validated PLD3 knockout cell lines, clone 3 ($PLD3^{-/-}$) and clone 14 ($PLD3^{-/-c14}$),
353 in the SH-SY5Y neuroblastoma cell line, as shown in Fig. S1.
354 Lysosomal attributes in these cells, including size, density, and confluency, were characterized
355 by transmission electron microscopy (TEM) (Fig. 2A). The size of individual lysosomes in
356 $PLD3^{-/-}$ cells was enlarged by 48% compared to WT cells (Fig. 2A). Lysosomal density and
357 confluency, expressed by the number of lysosomes per unit area and the percentage of occupied
358 area, respectively, were also increased in the $PLD3^{-/-}$ lines (Fig. 2A).
359 Relative lysosomal pH was evaluated using the ratio of two fluorophores, Oregon Green (pH-
360 sensitive) and $Alexa^{594}$ (pH-insensitive), which were trafficked to lysosomes by conjugation to
361 dextran (Fig. 2B and Fig. S8). Dextran localization to lysosomes was confirmed by
362 colocalization and correlation analysis between the dextran signal and LAMP1-RFP (Fig. 2B and
363 Fig. S8A). We did not observe a significant change in the pH of lysosomes in $PLD3^{-/-}$ cells (Fig.
364 2B and Fig. S8A). Lysosome size increased by 61% (in line with the TEM result), and
365 confluency also increased in this fluorescence assay (Fig. S8A). Based on lysosomal labelling
366 with dextran, lysosome density was unchanged (Fig. S8A). Lysosome-related cellular processes,
367 such as endocytosis and autophagy, were enhanced by 2.5-fold and 2-fold respectively in $PLD3^{-/-}$
368 cells (Fig. 2B-C).
369 To assess changes in the lysosomal proteome, we isolated lysosomes from WT and $PLD3^{-/-}$ cells
370 using dextran-coated superparamagnetic iron oxide (SPIO) nanoparticles and magnetic
371 chromatography, followed by label-free proteomic studies on the lysates of lysosomal fractions.
372 Cathepsin D (CTSD), cathepsin B (CTSB), and LAMP2 were highly enriched in the lysosomes
373 of $PLD3^{-/-}$ cells as compared to WT cells (Fig. 2D), while cytosolic-proteins like β-tubulin were
374 appropriately absent in the lysosomal fraction (Fig. 2D).

375 Proteomic analysis of lysosomal lysates from each cell line identified 3,075 proteins, of which 81
376 were significantly upregulated and 72 were downregulated in PLD3$^{-/-}$ lines compared to WT
377 cells (Fig. 2E). Gene set enrichment analysis (GSEA) revealed that signaling pathways related to
378 lysosomal biogenesis, endocytosis, and calcium signaling were significantly enriched in PLD3$^{-/-}$
379 compared to WT cells (Fig. 2E-G and Fig. S9). PLD3$^{-/-}$ cells were also enriched in vesicle
380 trafficking proteins, such as SNARE (Soluble NSF Attachment Protein Receptor) proteins. We
381 also observed that proteins related to sphingolipid metabolism and proteins relevant to AD were
382 differentially enriched between WT and PLD3$^{-/-}$ cells (Fig. 2G).
383 We then examined the impact of PLD3 deficiency on the cellular transcriptome. Total RNA from
384 WT and PLD3$^{-/-}$ cells underwent RNA sequencing, followed by differential gene expression
385 (DGE) analysis and gene set enrichment analysis (GSEA). The sequencing data was summarized
386 into 60,662 genes, of which 7,673 genes were differentially expressed between WT and PLD3$^{-/-}$
387 cells, with 4,015 upregulated and 3,658 downregulated (FDR<0.05; (Fig. S10). The upregulated
388 genes were primarily associated with signaling pathways involved in cell-cell interaction, neural
389 development, and inflammatory conditions (Fig. S10). Signaling pathways related to lysosomal
390 biogenesis, endocytosis, and AD were also upregulated in PLD3$^{-/-}$ cells compared to WT cells.
391 However, their significance did not reach the FDR<10% threshold (Fig. S10).
392 To explore the immediate transcriptomic changes associated with the milder phenotype resulting
393 from PLD3 deficiency, PLD3 was knocked down in SH-SY5Y cells using siRNA, followed by
394 RNA sequencing and analysis, and verification through western blot (Fig. S11). Compared to
395 control siRNAs (CTL), all three PLD3 siRNAs achieved 60-90% knockdown of PLD3 (Fig.
396 S11). DGE analysis revealed 2,830 genes that were differentially expressed between PLD3 KD
397 and CTL cells (Fig. S11). 2,118 genes were upregulated, and 712 genes were downregulated in

398 PLD3 KD cells compared to CTL cells (FDR<0.05; Fig. S11). We also observed significant
399 enrichment in signaling pathways associated with lysosomes and autophagic flux, such as
400 lysosome biogenesis, endocytosis, mTOR signaling, and autophagy signaling, in PLD3 KD cells
401 relative to CTL cells (Fig. 2H). Additionally, signaling pathways previously reported to be
402 associated with PLD3 or lysosomes were also differentially enriched between PLD3 KD cells
403 and CTL cells (Fig. 2H). The transcripts associated with lysosome biogenesis and AD
404 pathologies are illustrated in Fig. 2I and 2J, showing a significant increase in PLD3 KD cells
405 compared to CTL cells.
406
407 **Loss of PLD3 increases CTSB level and activity and alters its subcellular location.**
408 Because both synthetic and human brain-derived β-amyloid seeds decrease PLD3 levels, and
409 PLD3$^{-/-}$ in SH-SY5Y cells altered the level of some lysosome resident protein, particularly
410 CTSB, we evaluated CTSB levels in WT and PLD3$^{-/-}$ cells exposed to synthetic Aβ_{1-42} (1 μg/ml)
411 for 1, 3, 5, and 7 days (Fig. 3A). Mature CTSB (MatCTSB) levels were increased in WT and
412 PLD3$^{-/-}$ cells after exposure to Aβ_{1-42}. This increase was more substantial and sustained in PLD3^{-}
413 $^{/-}$ cells (Fig. 3A). Additionally, we found that PLD3$^{-/-}$ cells had increased specific CTSB activity
414 compared to WT cells (Fig. 3B). However, increased CTSB activity did not lead to improved
415 lysosomal degradative capacity as measured by DQ assay (Fig. 3C). PLD3$^{-/-}$ cells treated with β-
416 amyloid particles isolated from human brain had an accumulation of intracellular β-amyloid
417 compared to wild type cells after a three-day incubation. Similarly, human synthetic alpha-
418 synuclein accumulated in PLD3$^{-/-}$ cells compared to wild type cells (Fig. 3C). PLD3$^{-/-}$ cells were
419 able to degrade synthetic Aβ_{1-42} to the same extent as WT (Fig. 3C).

420 In human brain homogenates of superior temporal gyrus grey matter, pro-cathepsin B
421 (ProCTSB) and mature cathepsin B (MatCTSB) were detectable at ~43-46 kDa and 25-26 kDa,
422 respectively (Fig. 3D and S14). We found an increase in MatCTSB level in AD compared to
423 non-AD cases when levels were normalized to the neuronal marker NeuN or to GADPH (Fig. 3D
424 and S13).
425 Since a change in subcellular CTSB location may also contribute to the deficit in the hydrolysis
426 of protein aggregates despite increasing overall CTSB level and activity, we measured the
427 colocalization of CTSB with lysosomal marker LAMP2 in the cell model and in human brain
428 tissue. We found a reduction of CTSB co-localization with LAMP2 in PLD3$^{-/-}$ cells incubated
429 with Aβ_{1-42} (1 μg/ml) for 7-days compared to untreated PLD3$^{-/-}$ cells, but not in treated WT cells
430 compared to untreated WT cells (Fig. 3E). Likewise, a significant portion of CTSB is not
431 colocalized to lysosomes in AD brain tissue but is instead localized in the extra-lysosomal
432 compartment (Fig. 3F and Fig. S14A-B). This extracellular localization included the human
433 brain microvasculature. We stained CTSB and collagen-IV; CTSB staining was present in the
434 vasculature in control cases but was much more abundant in AD cases, especially in those with
435 CAA (Fig. 3G and Fig. S14C-D). To confirm this association, we isolated human vessels from
436 the superior temporal lobe and measured CTSB levels, revealing an increase in CTSB in AD
437 compared to non-AD (Fig. 3H).
438
439 **PLD3 regulates TFEB/TFE3 degradation through the proteasome rather than lysosomes.**
440 Based on our proteomic analysis of isolated lysosomes from PLD3$^{-/-}$ cells, we hypothesized that
441 PLD3 might play a role in lysosomal biogenesis. We assessed mRNA levels of TFEB and TFE3
442 and found no significant difference between WT and PLD3$^{-/-}$ cells, suggesting that any potential

443 regulation of TFEB and TFE3 by PLD3 does not occur at the transcriptional level (Fig. S15A).
444 In contrast, TFEB and TFE3 protein levels were markedly elevated in PLD3$^{-/-}$ cells compared to
445 WT cells under a range of conditions including no stimulation (NS), dextran treatments to induce
446 endocytosis, nutrient starvation (HBSS), and Torin 1 treatment to induce autophagy (Fig. 4A and
447 Fig. S15B). Exogenous TFEB, expressed as GFP N-terminal tagged TFEB, also showed
448 increased expression in PLD3$^{-/-}$ cells versus WT cells (Fig. 4B). We found that in both PLD3
449 knockdown (KD) and in PLD3$^{-/-}$ cells, the expression trends in TFEB and TFE3 were similar
450 (Fig. S15C). Consistent with these results, the overexpression of PLD3 in HeLa cells led to a
451 significant reduction in TFEB and TFE3 levels (Fig. 4C). Interestingly, AD-associated variants
452 in PLD3, e.g., V232M or K486R, did not alter its effects on TFEB metabolism (Fig. 4C). These
453 data suggest that PLD3 is involved in TFEB/TFE3 protein metabolism, and PLD3$^{-/-}$ leads to their
454 accumulation.
455 We investigated the potential involvement of the proteasome and/or lysosome in PLD3
456 regulation of TFEB/TFE3 degradation. Treatment with MG132, a proteasome inhibitor, caused a
457 significant accumulation of TFE3 and resulted in comparable levels of TFE3 between WT and
458 PLD3$^{-/-}$ cells at all three time points (Fig. 4D), suggesting that PLD3 facilitates TFE3
459 degradation via the proteasome. In contrast, TFEB levels declined over time following MG132
460 treatment, indicating that the proteasome was indirectly involved in PLD3-mediated TFEB
461 metabolism (Fig. 4D). Treatment with another proteasome inhibitor, bortezomib, produced
462 similar effects on TFEB/TFE3 (Fig. S16A). To focus on protein metabolism, we blocked protein
463 translation using cycloheximide (CHX) and assessed TFEB/TFE3 levels following MG132
464 treatment. MG132 generated similar effects on TFEB/TFE3 with the arrest of protein translation,
465 supporting the conclusion that the proteasome is involved in PLD3-mediated TFEB/TFE3

466 protein metabolism (Fig. S16A). Interestingly, CHX treatment led to a sharp decline in TFE3
467 levels but a gradual decrease in PLD3 and TFEB levels, suggesting that TFE3 is a short-lived
468 protein, while TFEB and PLD3 are long-lived proteins (Fig. S17A). Immunoprecipitated (IP)
469 TFE3 showed heightened ubiquitination in WT cells versus PLD3$^{-/-}$ cells upon MG132 treatment
470 (Fig. S17B). Concerning the potential involvement of lysosomes in TFEB/TFE3 metabolism,
471 treatments with lysosome alkalinizing agents, chloroquine (CQ) or bafilomycin A1 (BAF),
472 exhibited no significant effects on TFEB/TFE3 levels, which suggests that these proteins are not
473 predominantly degraded via lysosomal pathways (Fig. 4E and 4F). Nevertheless, we did observe
474 an accumulation of TFE3 after prolonged exposure to CQ or BAF. This could be due to the
475 induction of lysosomal stress following CQ or BAF exposure, which activated TFE3 signaling
476 rather than directly impacting TFE3 protein metabolism (Fig. 4E and 4F).
477 TFEB levels in the brains of AD patients were significantly higher than in non-AD patients (Fig.
478 4G). However, this pattern was not observed for TFE3 (Fig. 4G).
479
480 **Loss of PLD3 enhances nuclear translocation and transcriptional activity of TFEB/TFE3.**
481 To determine whether the change in TFEB/TFE3 protein levels in PLD3$^{-/-}$ cells altered
482 TFEB/TFE3 signaling, we assessed TFEB/TFE3 levels in the cytoplasmic *(c)* and nuclear *(n)*
483 compartments using western blotting. Under basal conditions and conditions known to induce
484 autophagy, including nutrient deprivation (HBSS) or mTOR inhibition (Torin 1), the protein
485 levels of TFEB/TFE3 in the nuclear compartment of PLD3$^{-/-}$ cells were much higher than those
486 in WT cells (Fig. 5B). However, we did not find a significant difference in the protein ratio of
487 nuclear TFEB/TFE3 to cytosolic TFEB/TFE3 between WT and PLD3$^{-/-}$ cells (Fig. 5B).
488 Surprisingly, we observed some nuclear localization of PLD3 in WT cells (Fig. 5A).

489 Immunocytochemical staining of TFEB confirmed these findings, showing increased TFEB
490 levels and nuclear translocation in PLD3$^{-/-}$ cells compared to WT cells (Fig. S18). Exogenous
491 TFEB, expressed as GFP N-terminal tagged TFEB, also exhibited increased nuclear
492 translocation in PLD3$^{-/-}$ cells versus WT cells, with or without Torin 1 treatment (Fig. S18).
493 Corresponding to the increased nuclear translocation of TFEB/TFE3, the transcription of their
494 targeted genes, which contain coordinated lysosomal expression and regulation (CLEAR) motif,
495 was also augmented (Fig. 5D) in PLD3$^{-/-}$ cells compared to WT cells. Moreover, the mRNA
496 levels of two genes, RRAGD and GPNMB, known to respond to TFEB, were upregulated (Fig.
497 5E).
498 Next, we examined TFEB/TFE3 signaling in neuroblastoma cells after exposure to synthetic
499 Aβ_{1-42} at various intervals. In WT and PLD3$^{-/-}$ cells, Aβ_{1-42} exposure mediated TFEB and TFE3
500 nuclear translocation from day 3 through day 7 (Fig. 5F). The nuclear translocation of TFEB and
501 TFE3 in response to Aβ_{1-42} exposure was much higher in PLD3$^{-/-}$ cells than in WT cells (Fig.
502 5F).
503

504 **Discussion**

505 This study links PLD3 to lysosome abnormalities in AD. PLD3 levels were reduced in human
506 AD by 38% compared to non-AD human brains. In cultured cells, PLD3 deficiency resulted in
507 changes in lysosomal morphology, biogenesis, and degradative function, while lysosomal
508 acidification remained relatively intact. These findings are significant given the pivotal role of
509 the endosomal and lysosomal systems in proteinopathies.
510 We and others previously described the distribution of PLD3 in histological staining of human
511 brain tissue, reporting that it is primarily in neuronal lysosomes and enriched in dystrophic

512 neurites around neuritic plaques (20, 21). In the current study, we further characterized the level
513 and distribution of PLD3 in white versus grey matter across multiple brain regions to refine our
514 understanding of its association with the neuropathologies of AD. Our observations in cell
515 models suggest that Aβ exposure may contribute to the reduced level of PLD3 we observed in
516 neurons. In line with diminished PLD3 in AD cortex, ubiquitination of PLD3 was markedly
517 increased in AD tissue. PLD3-ubiquitin complexes were primarily non-lysosomal and frequently
518 colocalized with neurofibrillary tangles and neuropil threads. This is consistent with a previous
519 finding from a cellular model system showing that ubiquitinated PLD3 fails to traffic to the
520 lysosome (42).
521 Cultured neuroblastoma (SH-SY5Y) cells with PLD3 deletion had numerous lysosomal
522 abnormalities including lysosomal enlargement and decreased efficiency in processing
523 aggregated α-synuclein and β-amyloid particle derived from human brain tissue. There was no
524 difference in the cells' ability to degrade synthetic $A\beta_{1-42}$, but this may be due to differences in
525 aggregate size, endocytosis rate, or a number of other factors. There was a general pattern of
526 impaired degradative function in $PLD3^{-/-}$ lysosomes. In line with this result, we found the
527 proteolytic capacity of the cells was compromised based on the DQ assay. In contrast with these
528 findings, we found that the enzymatic activity of CTSB and the level of both CTSD and CTSB
529 were increased in PLD3-/- cells.
530 We isolated lysosomes from these cells using magnetic chromatography and performed ICP-MS
531 to characterize the lysosomal proteome. We confirmed that the lysosomes also had elevated
532 levels of CTSB, LAMP1 and 2, Hex A and B, β-galactosidase, and CD63, among numerous
533 other lysosomal proteins. We also found that signaling pathways relevant to AD were enriched in
534 $PLD3^{-/-}$ lysosomes, including elevations in presenilin 2 and LRP1. This broad alteration in the

535 proteome led us to hypothesize that PLD3 may alter proteolytic lysosome machinery and have a
536 role in regulating lysosomal biogenesis.
537 We also discovered that in differentiated PLD3$^{-/-}$ neurons stressed by prolonged exposure to β-
538 amyloid, the fraction of CTSB associated with lysosomes was decreased, despite increased total
539 levels of CTSB. We also observed extra-lysosomal CTSB in neurons and in extracellular
540 matrices in human AD cortex. The loss of lysosomal localization of CTSB may account for the
541 increase in CTSB activity in PLD3$^{-/-}$ neurons, while total lysosomal degradative capacity was
542 decreased. CTSB may be leaking from damaged/enlarged lysosomes into extra-lysosomal
543 compartments. CTSB is primarily localized to neuronal lysosomes in non-disease conditions, but
544 CTSB leakage from injured lysosomes can lead to apoptosis (4) and pyroptosis mediated by
545 caspase-1(44). Recent studies have found that CTSB may be enzymatically active in
546 extralysosomal locations, including the nucleus (45) and extracellular space (46-48), because , in
547 contrast with other lysosomal proteases, CTSB retains proteolytic activity at neutral pH (49, 50).
548 This activity at neutral pH is key to CTSB-mediated adverse effects in the cytoplasm (44, 51-54)
549 and the degradation of matrix components in the extracellular space (55-57). Our results suggest
550 that loss of PLD3 not only regulates CTSB abundance but may contribute to loss of its lysosomal
551 localization.
552 We next confirmed that PLD3 has a role in regulating lysosomal biogenesis by demonstrating
553 that TFEB was markedly elevated in the PLD3$^{-/-}$ cells. TFEB and TFE3 are master regulators of
554 lysosomal biogenesis and autophagy; their role as transcription factors for lysosome-related
555 genes activates lysosome production (58-60). Unlike conventional lysosomal stressors, such as
556 amino acid deprivation, the deletion of PLD3 did not significantly impact mTOR and calcineurin
557 activity. The phosphorylation level of endogenous TFEB at Ser^{142} and Ser^{211} was undetectable in

558 SH-SY5Y cells. However, we observed a marked increase in TFEB and TFE3 protein levels (but
559 not mRNA levels), and a corresponding increase in nuclear TFEB/TFE3 levels upon PLD3
560 knockout, suggesting that PLD3 regulates TFEB/TFE3 metabolism at the protein level. We
561 assessed whether PLD3 mediated the degradation of TFEB and TFE3 via the proteasome. While
562 treatment with proteasome inhibitors increased TFE3 levels, TFEB levels significantly fell with
563 proteasome inhibition.
564 Additionally, while ubiquitin-mediated degradation of TFEB via the proteasome has been
565 reported to be initiated by phosphorylation of TFEB by the IKK complex (61), our study did not
566 show significant changes in IKKα/β, and the level of phosphorylated TFEB was undetectable in
567 our cellular models (Fig. S16C and D). We speculate that TFEB is regulated by one or more
568 proteins metabolized through the proteasome, but further studies are needed to delineate the
569 mechanisms by which the proteasome influences TFEB metabolism. Moreover, because PLD3 is
570 primarily localized in lysosomes (9), it will be essential to identify the mediators that transmit
571 signals from lysosomes to TFEB and TFE3.

572 **Conclusion**

573 PLD3 has a regulatory role in neuronal lysosomal function and biogenesis. Loss of PLD3
574 reduces lysosomal degradative function and may permit cathepsin B trafficking to extra-
575 lysosomal compartments. Loss of PLD3 also promotes neuronal biogenesis by increasing the key
576 transcription factors TFEB and TFE3. Consequently, restoring neuronal PLD3 levels may be an
577 experimental approach to improving neuronal proteostasis in AD.

578

579 **Acknowledgements**

580 We thank the many patients and their families who have donated brain tissue to support this and
581 other necessary studies. We also acknowledge the contributions of the Vanderbilt Cell Imaging
582 Shared Resource (CISR) Core for transmission electron microscopy, the Vanderbilt
583 Technologies for Advanced Genomics (VANTAGE) Core for RNA sequencing, and the Mass
584 Spectrometry Research Center for proteomic analysis.
585 We also acknowledge the contributions of Drs. Ketaki A. Katdare and Ethan S. Lippmann for
586 providing the IPSC-neurons cells.

587 **Author contributions**

588 The authors confirm specific contribution to the paper as follows: study conception and design:
589 W.R-F., Y.W., C.C-T and M.S.S. PLD3 expression, distribution, and post-translational
590 modification in PLD3$^{-/-}$cells and brain tissues; CTSB level, activity, and localization changes in
591 PLD3$^{-/-}$ cells and brain tissues; and assays for intracellular accumulation of amyloid and α-
592 synuclein. W.R-F, C.C-T, S.J., E.W, A.P, T.A., A.K., A.S, N.H, . S.J.F, and V.A.J performed the
593 corresponding experimental work and data collection, as presented in Figures 1 and 3 and
594 Supplementary Figures 1, 2, 3, 4, 5, 7, 13, and 14. Analyses of lysosomal morphology, and
595 function in PLD3$^{-/-}$ cells or brain tissues; proteomic profiling of lysosomal proteins; whole-cell
596 RNA-seq transcriptomic profiling and related computational analyses; and mechanistic studies
597 elucidating the link between PLD3, amyloid and TFEB/TFE3 signaling and metabolism: Y.W.,
598 P.R., and N.A. performed the corresponding experimental work and data collection, as presented
599 in Figures 2, 4, and 5 and Supplementary Figures 6, 8, 9, 10, 11, 12, and 15-18. W.R-F and MSS
600 supervised the study. Analysis and interpretation of results, draft manuscript preparation, and
601 substantial revision: W.R-F., Y.W., S.J., E.W., A.P., L.V-A., N.H., T.J.H., B.C.M., J.A.M., and

M.S.S. All authors contributed to the final revision of the manuscript and approved the version submitted for publication.

Funding

This project is financially supported by grants from the National Institutes of Health (1R56AG074279, 1K76AG060001) and a National Institutes of Health training grant (5T32AG058524) to M.S.S, and a R35GM144112 to J.A.M.

Data availability statement

The data supporting this study's findings are available from the corresponding author upon reasonable request.

Competing interests

MSS has received research support from the NIH (1RF1NS129735, R01AG078803, RF1NS130334, and R21AG070859), American Federation of Aging Research (K76AG060001/Beeson Scholar), the NeuroScience Innovation Foundation. He has received payments for consulting from Greycourt and Co, Inc, Guidepoint, Raymond James Financial, Inc, and has received payments for expert testimony in legal cases. He chairs the DSMB for the REVISION trial, serves on the medical advisory board for Septagen and is the research integrity officer for the Journal of Alzheimer's Disease. TH serves on the scientific advisory board for Circular Genomics and serves as the Deputy Editor for Alzheimer's & Dementia: TRCI

The rest of authors declare no competing interests.

References

1. Hampel H, Frank R, Broich K, Teipel SJ, Katz RG, Hardy J, et al. Biomarkers for Alzheimer's disease: academic, industry and regulatory perspectives. Nat Rev Drug Discov. 2010;9(7):560–74.
2. Braak H, Braak E. Neuropathological stageing of Alzheimer-related changes. Acta Neuropathol. 1991;82(4):239–59.
3. Hershko A, Ciechanover A. The ubiquitin system. Annu Rev Biochem. 1998;67:425–79.
4. Boland B, Yu WH, Corti O, Mollereau B, Henriques A, Bezard E, et al. Promoting the clearance of neurotoxic proteins in neurodegenerative disorders of ageing. Nat Rev Drug Discov. 2018;17(9):660–88.
5. Upadhya SC, Hegde AN. Role of the ubiquitin proteasome system in Alzheimer's disease. BMC Biochem. 2007;8 Suppl 1:S12.
6. Abreha MH, Dammer EB, Ping L, Zhang T, Duong DM, Gearing M, et al. Quantitative Analysis of the Brain Ubiquitylome in Alzheimer's Disease. Proteomics. 2018;18(20):e1800108.
7. Komatsu M, Waguri S, Chiba T, Murata S, Iwata J, Tanida I, et al. Loss of autophagy in the central nervous system causes neurodegeneration in mice. Nature. 2006;441(7095):880–4.
8. Nixon RA. The aging lysosome: An essential catalyst for late-onset neurodegenerative diseases. Biochim Biophys Acta Proteins Proteom. 2020;1868(9):140443.
9. Menzies FM, Fleming A, Rubinsztein DC. Compromised autophagy and neurodegenerative diseases. Nature Reviews Neuroscience. 2015;16(6):345–57.
10. Tan JX, Finkel T. Lysosomes in senescence and aging. Embo Rep. 2023;24(11).
11. Xu H, Ren D. Lysosomal physiology. Annu Rev Physiol. 2015;77:57–80.
12. Lee JH, Yang DS, Goulbourne CN, Im E, Stavrides P, Pensalfini A, et al. Faulty autolysosome acidification in Alzheimer's disease mouse models induces autophagic build-up of Abeta in neurons, yielding senile plaques. Nat Neurosci. 2022;25(6):688–701.
13. Settembre C, Di Malta C, Polito VA, Garcia-Arencibia M, Vetrini F, Erdin S, et al. TFEB Links Autophagy to Lysosomal Biogenesis. Science. 2011;332(6036):1429–33.
14. Roczniak-Ferguson A, Petit CS, Froehlich F, Qian S, Ky J, Angarola B, et al. The transcription factor TFEB links mTORC1 signaling to transcriptional control of lysosome homeostasis. Sci Signal. 2012;5(228):ra42.
15. Gu ZY, Cao H, Zuo CC, Huang YQ, Miao JF, Song Y, et al. TFEB in Alzheimer's disease: From molecular mechanisms to therapeutic implications. Neurobiology of Disease. 2022;173.
16. Zhang W, Li X, Wang S, Chen Y, Liu H. Regulation of TFEB activity and its potential as a therapeutic target against kidney diseases. Cell Death Discov. 2020;6:32.
17. Wright R. Lysosome regulation of microglia in Alzheimer's disease via TFEB-vacuolar ATPase. Nature Neuroscience. 2024;27(1):13–4.
18. Gonzalez AC, Stroobants S, Reisdorf P, Gavin AL, Nemazee D, Schwudke D, et al. PLD3 and spinocerebellar ataxia. Brain. 2018;141.
19. Nibbeling EAR, Duarri A, Verschuuren-Bemelmans CC, Fokkens MR, Karjalainen JM, Smeets CJLM, et al. Exome sequencing and network analysis identifies shared mechanisms underlying spinocerebellar ataxia. Brain. 2017;140:2860–78.
20. Satoh J, Kino Y, Yamamoto Y, Kawana N, Ishida T, Saito Y, et al. PLD3 is accumulated on neuritic plaques in Alzheimer's disease brains. Alzheimers Res Ther. 2014;6(9):70.

667 21. Nackenoff AG, Hohman TJ, Neuner SM, Akers CS, Weitzel NC, Shostak A, et al. PLD3
668 is a neuronal lysosomal phospholipase D associated with beta-amyloid plaques and cognitive
669 function in Alzheimer's disease. PLoS Genet. 2021;17(4):e1009406.
670 22. Yuan P, Zhang M, Tong L, Morse TM, McDougal RA, Ding H, et al. PLD3 affects
671 axonal spheroids and network defects in Alzheimer's disease. Nature. 2022;612(7939):328–37.
672 23. Fazzari P, Horre K, Arranz AM, Frigerio CS, Saito T, Saido TC, et al. PLD3 gene and
673 processing of APP. Nature. 2017;541(7638):E1–E2.
674 24. Singh S, Dransfeld UE, Ambaw YA, Lopez-Scarim J, Farese RV, Jr., Walther TC. PLD3
675 and PLD4 synthesize S,S-BMP, a key phospholipid enabling lipid degradation in lysosomes.
676 Cell. 2024;187(24):6820–34 e24.
677 25. Gavin AL, Huang D, Blane TR, Thinnes TC, Murakami Y, Fukui R, et al. Cleavage of
678 DNA and RNA by PLD3 and PLD4 limits autoinflammatory triggering by multiple sensors. Nat
679 Commun. 2021;12(1):5874.
680 26. Romero-Fernandez W, Carvajal-Tapia C, Prusky A, Katdare KA, Wang E, Shostak A, et
681 al. Detection, visualization and quantification of protein complexes in human Alzheimer's
682 disease brains using proximity ligation assay. Sci Rep. 2023;13(1):11948.
683 27. Romero-Fernandez W, Borroto-Escuela DO, Vargas-Barroso V, Narvaez M, Di Palma
684 M, Agnati LF, et al. Dopamine D1 and D2 receptor immunoreactivities in the arcuate-median
685 eminence complex and their link to the tubero-infundibular dopamine neurons. Eur J Histochem.
686 2014;58(3):2400.
687 28. Ventura-Antunes L, Nackenoff A, Romero-Fernandez W, Wang Y, Bosworth AM,
688 Prusky A, et al. Arteriolar degeneration and stiffness in cerebral amyloid angiopathy are linked
689 to Abeta deposition and lysyl oxidase. Alzheimers Dement. 2025;21(6):e70254.
690 29. Borroto-Escuela DO, Romero-Fernandez W, Garriga P, Ciruela F, Narvaez M,
691 Tarakanov AO, et al. G protein-coupled receptor heterodimerization in the brain. Methods
692 Enzymol. 2013;521:281–94.
693 30. Borroto-Escuela DO, Hagman B, Woolfenden M, Pinton L, Jiménez-Beristain A, Oflijan
694 J, et al. In Situ Proximity Ligation Assay to Study and Understand the Distribution and Balance
695 of GPCR Homo- and Heteroreceptor Complexes in the Brain. In: Luján R, Ciruela F, editors.
696 Receptor and Ion Channel Detection in the Brain: Methods and Protocols. New York, NY:
697 Springer New York; 2016. p. 109–24.
698 31. Xu F, Fu Z, Dass S, Kotarba AE, Davis J, Smith SO, et al. Cerebral vascular amyloid
699 seeds drive amyloid beta-protein fibril assembly with a distinct anti-parallel structure. Nat
700 Commun. 2016;7:13527.
701 32. Shipley MM, Mangold CA, Szpara ML. Differentiation of the SH-SY5Y Human
702 Neuroblastoma Cell Line. J Vis Exp. 2016(108):53193.
703 33. Kumar KK, Lowe EW, Jr., Aboud AA, Neely MD, Redha R, Bauer JA, et al. Cellular
704 manganese content is developmentally regulated in human dopaminergic neurons. Sci Rep.
705 2014;4:6801.
706 34. Shi Y, Kirwan P, Livesey FJ. Directed differentiation of human pluripotent stem cells to
707 cerebral cortex neurons and neural networks. Nat Protoc. 2012;7(10):1836–46.
708 35. O'Grady BJ, Balotin KM, Bosworth AM, McClatchey PM, Weinstein RM, Gupta M, et
709 al. Development of an N-Cadherin Biofunctionalized Hydrogel to Support the Formation of
710 Synaptically Connected Neural Networks. ACS Biomater Sci Eng. 2020;6(10):5811–22.

711 36. Howard GC, Wang J, Rose KL, Jones C, Patel P, Tsui T, et al. Ribosome subunit attrition
712 and activation of the p53-MDM4 axis dominate the response of MLL-rearranged cancer cells to
713 WDR5 WIN site inhibition. Elife. 2024;12.
714 37. Cox J, Hein MY, Luber CA, Paron I, Nagaraj N, Mann M. Accurate proteome-wide
715 label-free quantification by delayed normalization and maximal peptide ratio extraction, termed
716 MaxLFQ. Mol Cell Proteomics. 2014;13(9):2513–26.
717 38. Choi M, Chang CY, Clough T, Broudy D, Killeen T, MacLean B, et al. MSstats: an R
718 package for statistical analysis of quantitative mass spectrometry-based proteomic experiments.
719 Bioinformatics. 2014;30(17):2524–6.
720 39. Bray NL, Pimentel H, Melsted P, Pachter L. Near-optimal probabilistic RNA-seq
721 quantification. Nat Biotechnol. 2016;34(5):525–7.
722 40. Love MI, Huber W, Anders S. Moderated estimation of fold change and dispersion for
723 RNA-seq data with DESeq2. Genome Biol. 2014;15(12):550.
724 41. Subramanian A, Tamayo P, Mootha VK, Mukherjee S, Ebert BL, Gillette MA, et al.
725 Gene set enrichment analysis: a knowledge-based approach for interpreting genome-wide
726 expression profiles. Proc Natl Acad Sci U S A. 2005;102(43):15545–50.
727 42. Gonzalez AC, Schweizer M, Jagdmann S, Bernreuther C, Reinheckel T, Saftig P, et al.
728 Unconventional Trafficking of Mammalian Phospholipase D3 to Lysosomes. Cell Rep.
729 2018;22(4):1040–53.
730 43. Cruchaga C, Karch CM, Jin SC, Benitez BA, Cai Y, Guerreiro R, et al. Rare coding
731 variants in the phospholipase D3 gene confer risk for Alzheimer's disease. Nature.
732 2014;505(7484):550–4.
733 44. Halle A, Hornung V, Petzold GC, Stewart CR, Monks BG, Reinheckel T, et al. The
734 NALP3 inflammasome is involved in the innate immune response to amyloid-beta. Nat
735 Immunol. 2008;9(8):857–65.
736 45. Hamalisto S, Stahl JL, Favaro E, Yang Q, Liu B, Christoffersen L, et al. Spatially and
737 temporally defined lysosomal leakage facilitates mitotic chromosome segregation. Nat Commun.
738 2020;11(1):229.
739 46. Padamsey Z, McGuinness L, Bardo SJ, Reinhart M, Tong R, Hedegaard A, et al.
740 Activity-Dependent Exocytosis of Lysosomes Regulates the Structural Plasticity of Dendritic
741 Spines. Neuron. 2017;93(1):132–46.
742 47. Verderio C, Cagnoli C, Bergami M, Francolini M, Schenk U, Colombo A, et al. TI-
743 VAMP/VAMP7 is the SNARE of secretory lysosomes contributing to ATP secretion from
744 astrocytes. Biol Cell. 2012;104(4):213–28.
745 48. Tran AP, Sundar S, Yu M, Lang BT, Silver J. Modulation of Receptor Protein Tyrosine
746 Phosphatase Sigma Increases Chondroitin Sulfate Proteoglycan Degradation through Cathepsin
747 B Secretion to Enhance Axon Outgrowth. J Neurosci. 2018;38(23):5399–414.
748 49. Mort JS, Recklies AD, Poole AR. Extracellular presence of the lysosomal proteinase
749 cathepsin B in rheumatoid synovium and its activity at neutral pH. Arthritis Rheum.
750 1984;27(5):509–15.
751 50. Linebaugh BE, Sameni M, Day NA, Sloane BF, Keppler D. Exocytosis of active
752 cathepsin B enzyme activity at pH 7.0, inhibition and molecular mass. Eur J Biochem.
753 1999;264(1):100–9.
754 51. Schotte P, Van Criekinge W, Van de Craen M, Van Loo G, Desmedt M, Grooten J, et al.
755 Cathepsin B-mediated activation of the proinflammatory caspase-11. Biochem Biophys Res
756 Commun. 1998;251(1):379–87.

757 52. Vancompernolle K, Van Herreweghe F, Pynaert G, Van de Craen M, De Vos K, Totty N,
758 et al. Atractyloside-induced release of cathepsin B, a protease with caspase-processing activity.
759 FEBS Lett. 1998;438(3):150–8.
760 53. Boya P, Andreau K, Poncet D, Zamzami N, Perfettini JL, Metivier D, et al. Lysosomal
761 membrane permeabilization induces cell death in a mitochondrion-dependent fashion. J Exp
762 Med. 2003;197(10):1323–34.
763 54. Duewell P, Kono H, Rayner KJ, Sirois CM, Vladimer G, Bauernfeind FG, et al. NLRP3
764 inflammasomes are required for atherogenesis and activated by cholesterol crystals. Nature.
765 2010;464(7293):1357–61.
766 55. Almeida PC, Nantes IL, Chagas JR, Rizzi CC, Faljoni-Alario A, Carmona E, et al.
767 Cathepsin B activity regulation. Heparin-like glycosaminogylcans protect human cathepsin B
768 from alkaline pH-induced inactivation. J Biol Chem. 2001;276(2):944–51.
769 56. Tu C, Ortega-Cava CF, Chen G, Fernandes ND, Cavallo-Medved D, Sloane BF, et al.
770 Lysosomal cathepsin B participates in the podosome-mediated extracellular matrix degradation
771 and invasion via secreted lysosomes in v-Src fibroblasts. Cancer Res. 2008;68(22):9147–56.
772 57. Vidak E, Javorsek U, Vizovisek M, Turk B. Cysteine Cathepsins and their Extracellular
773 Roles: Shaping the Microenvironment. Cells. 2019;8(3).
774 58. Martina JA, Diab HI, Lishu L, Jeong AL, Patange S, Raben N, et al. The nutrient-
775 responsive transcription factor TFE3 promotes autophagy, lysosomal biogenesis, and clearance
776 of cellular debris. Sci Signal. 2014;7(309):ra9.
777 59. Martina JA, Diab HI, Brady OA, Puertollano R. TFEB and TFE3 are novel components
778 of the integrated stress response. Embo Journal. 2016;35(5):479–95.
779 60. Raben N, Puertollano R. TFEB and TFE3: Linking Lysosomes to Cellular Adaptation to
780 Stress. Annu Rev Cell Dev Bi. 2016;32:255–78.
781 61. Yan Xiong JS, Meggie N. Young, Wen Xiong, Ali Jazayeri, Karl F. Poncha, Ma. Xenia
782 G. Ilagan, Qing Wang, Hui Zheng, Nicolas L. Young, Marco Sardiello. TFEB degradation is
783 regulated by an IKK/β-TrCP2 phosphorylation-ubiquitination cascade. 2023.
784
785

786

787 **Figure Legends.**

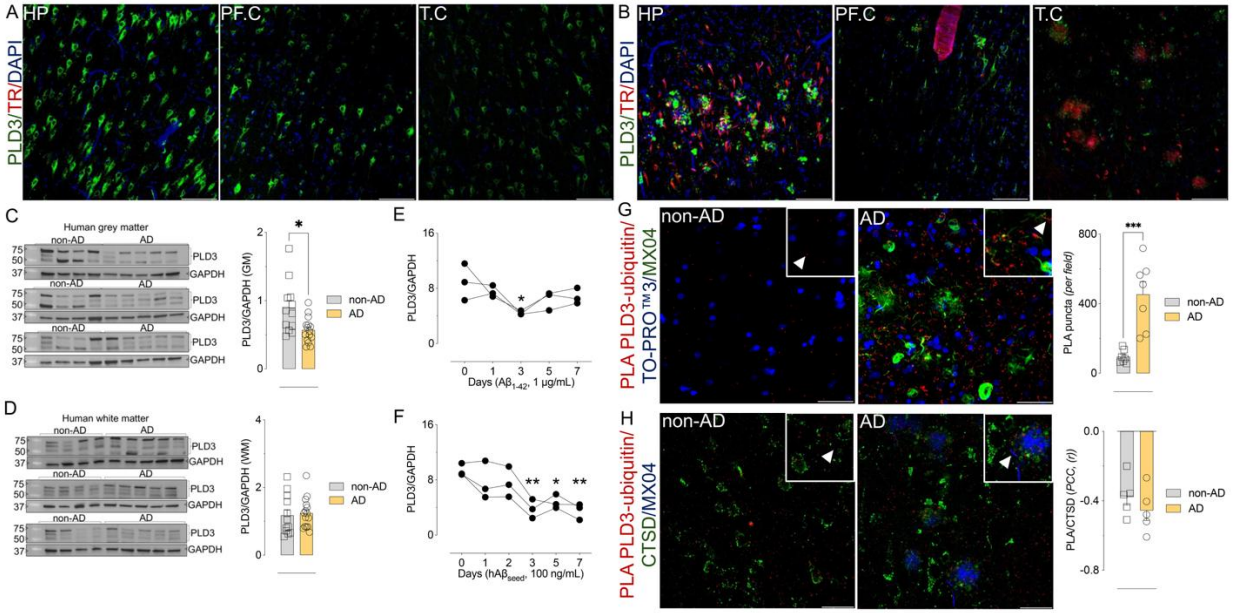

788

789 **Figure 1. PLD3 is decreased in human AD brain, likely due to ubiquitination.**

790 A and B) Immunostaining of PLD3 in the human brain. Representative confocal microscopy

791 images of PLD3 immunostaining *(green)* in the hippocampus (HP), posterior frontal (PF.C), and

792 superior temporal lobe (T.C) sections from (A) non-AD and (B) AD brain sections, *n=8.* Nuclei

793 were stained with DAPI *(blue),* and β-amyloid and neuritic plaques, neurofibrillary tangles, and

794 other tau aggregates were stained with Thiazine Red *(TR, red)*. The scale bars are 100 μm.

795 C and D) PLD3 levels. Western blot analysis of PLD3 in superior temporal lobe lysates from (C)

796 grey matter (GM) and (D) white matter (WM). Data are normalized to GADPH (means ±

797 S.E.M., non-AD *n=12*, and AD *n=15*). $^{*}p < 0.05$ by Welch's unequal variances *t*-test.

798 E) Outcome of 7-day incubation with synthetic $A\beta_{1-42}$ on PLD3 levels in SY-SY5Y-WT cells.

799 Data presented are normalized to GADPH (mean ± S.E.M., *n=3*). $^{*}p < 0.05$ by one-way ANOVA

800 compared to nontreated cells.

801 F) Outcome of 7-day incubation with brain-derived Aβ-seeds isolated from patients with CAA
802 on PLD3 levels in iPSC-neurons. Data presented are normalized to GADPH (mean ± S.E.M.,
803 *n=3*). $^{*}p < 0.05$, $^{**}p < 0.01$, $^{***}p < 0.001$ by one-way ANOVA compared to nontreated cells.
804 G) PLD3 ubiquitination is altered in AD as shown by representative confocal microscopy images
805 of complexes between PLD3 and ubiquitin *(in situ PLA, red clusters)* in non-AD *(left panel)* and
806 AD *(right panel)* sections, *n=7*. Data for quantification of PLA-puncta PLD3-ubiquitin
807 complexes *(per field)* is presented as mean ± S.E.M., *n=7* with five images per case. $^{***}p < 0.001$
808 by unpaired *t*-test. Nuclei were stained with TO-PRO™3 *(blue)* and AD hallmarks with MX04
809 *(green)*. The scale bars are 50 μm.
810 H) The subcellular location of PLD3-ubiquitin complexes is non-lysosomal. The correlation
811 coefficient of between PLA-puncta indicating PLD3-ubiquitin complexes and CTSD
812 immunostaining is anti-correlated. Pearson correlation coefficient *(PCC, r)* is presented as mean
813 ± S.E.M., *n=5*. The scale bars are 50 μm.
814
815

Figure 2. PLD3 deficiency alters the morphology and function of lysosomes.

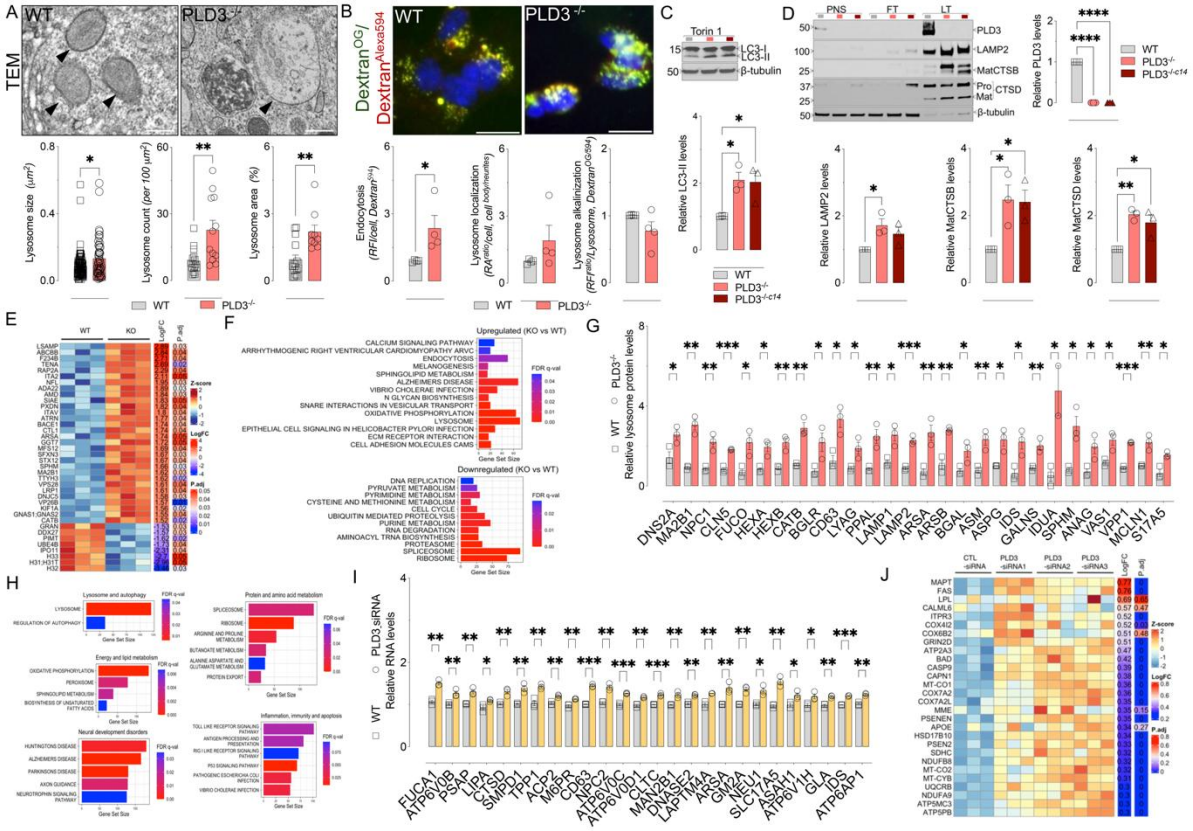

A) Quantification and comparison of lysosomal features *(size, density, and confluence)* between WT and PLD3$^{-/-}$ SHSY5Y cells by electron microscopy (TEM). Data presented mean ± S.E.M. For size: WT, *n=92* lysosomes; PLD3$^{-/-}$, *n=51* lysosomes ($^{*}p < 0.05$ by Welch's unequal variances *t*-test). For lysosome density (count per 100 μm^2): WT, *n=15* images; PLD3$^{-/-}$, *n=12* images ($^{**}p < 0.01$ Welch's unequal variances *t*-test). For lysosome count (occupied area): WT, *n=15* lysosomes; PLD3$^{-/-}$, *n=9* lysosomes ($^{**}p < 0.01$, Welch's unequal variances *t*-test). The scale bars are 500 nm.

B) We evaluated lysosomal features of lysosomal function *(endocytic activity, alkalinization, and positioning)* between WT and PLD3$^{-/-}$ cells incubated with Dextran^{OG} *(pH-sensitive)* and

827 dextran^{Alexa594} *(pH-insensitive)*. Data presented mean ± S.E.M., *n=4*. $^{*}p < 0.05$ by unpaired *t*-test.

828 The scale bars are 50 μm.

829 C) Western blot analysis of LC3-I and LC3-II in WT and PLD3$^{-/-}$ cells treated with Torin 1 (1

830 μM) for 3 hours. Proteins were quantified, expressed relative to β-tubulin, and compared

831 between phenotypes. Data presented means ± S.E.M., *n=3*. $^{*}p < 0.05$ by one-way ANOVA

832 followed by Dunnett's multiple comparisons test.

833 D) Lysosomal protein levels in lysosomes isolated from WT and PLD3$^{-/-}$ cells. Data presented

834 normalized to β-tubulin mean ± S.E.M., *n=3*. $^{*}p < 0.05$, $^{**}p < 0.01$, and $^{****}p < 0.0001$ by one-

835 way ANOVA followed by Dunnett's multiple comparison test. PNS: post-nuclear supernatant.

836 FT: flow-through. LF: lysosome fraction.

837 E) Proteomic analysis of the lysosomal lysates from WT and PLD3$^{-/-}$ cells. The differentially

838 expressed proteins were represented by a heatmap (*n=3*, minimum change in magnitude ≥ 1.5-

839 fold change, false discovery rate (FDR) less than 5% (< 0.05).

840 F) Normalized proteomic data were subject to gene set enrichment analysis (GSEA), and the

841 differentially regulated pathways in PLD3$^{-/-}$ versus WT were summarized and represented by bar

842 plots (FDR q value < 0.05).

843 G) Selected lysosomal proteins from the proteomic analysis were quantified and compared

844 between WT and PLD3$^{-/-}$, and the differentially regulated proteins were represented by bar

845 graphs (mean ± S.E.M., *n=3*, multiple unpaired *t*-tests).

846 H) RNA-Seq data underwent GSEA. Differentially enriched pathways in PLD3_siRNAs *(n=9)*

847 versus CTL_siRNA were summarized and represented by bar plots (FDR q value < 0.05).

848 I) RNA expression for genes related to lysosome pathways was calculated and compared

849 between CTL_siRNA *(n=3)* and PLD3_siRNAs *(n=9)*, and significantly different genes were

850 represented by bar graphs (mean ± SEM, multiple unpaired t test).

851 J) RNA expression in genes related to AD was calculated and compared between CTL_siRNA

852 *(n=3)* and PLD3_siRNAs *(n=9)*, and significantly different genes were represented by a heatmap

853 (mean ± SEM, multiple unpaired t test).

854

855

Figure 3. Loss of PLD3 triggers changes in CTSB level, activity, and subcellular location.

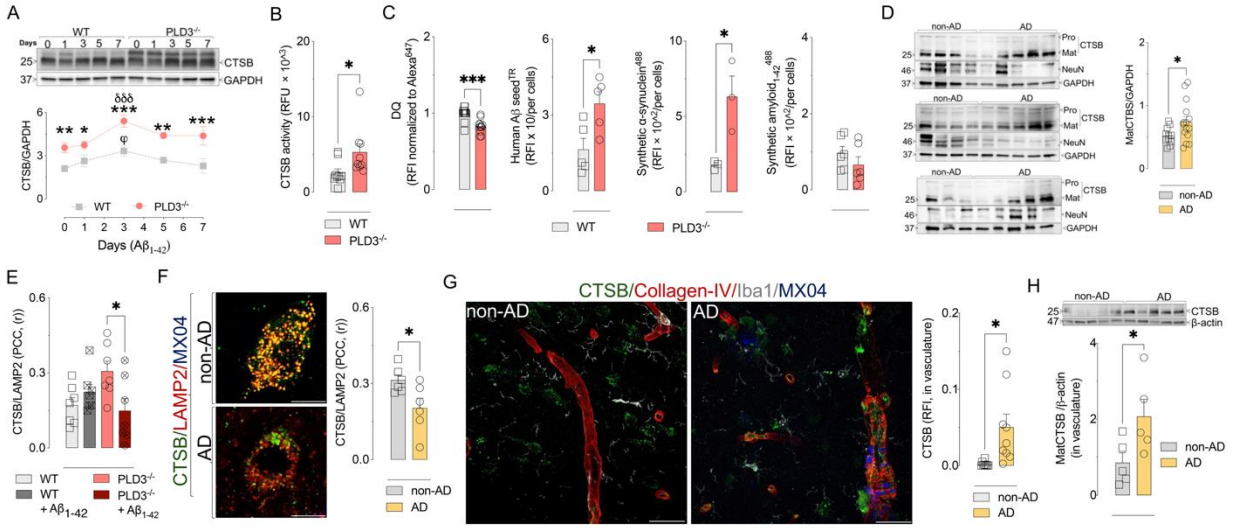

A) Outcome of long-term incubation with synthetic Aβ$_{1-42}$ (1 μg/mL) on CTSB levels in WT and PLD3$^{-/-}$ cells. Data presented mean ± S.E.M., *n=4*. $^{*}p < 0.05$, $^{**}p < 0.01$, and $^{***}p < 0.001$ by two-way ANOVA compared to WT. $^{\varphi}p < 0.05$ by one-way ANOVA compared to basal WT cells. $^{\delta\delta\delta}p < 0.001$ by one-way ANOVA compared to basal PLD3$^{-/-}$ cells.

B) Enzymatic CTSB activity in PLD3$^{-/-}$ cells compared to WT. Data normalized to enzymatic activity in the presence of the potent and selective inhibitor of CTSB, CA074 (1 μM). Data presented mean ± S.E.M., *n=9*. $^{*}p < 0.05$ by unpaired *t*-test.

C) Intracellular accumulation of protein aggregates in WT and PLD3$^{-/-}$ cells. Data presented mean ± S.E.M., *n=12 (for DQ), n=5 (for human Aβ seed^{TR}), n=3 (for human synthetic α-synuclein^{488}), and n=6 (for human synthetic Aβ$_{1-42}^{488}$)*. $^{*}p < 0.05$ and $^{***}p < 0.001$ by unpaired *t*-test.

E) Immuno-colocalization of CTSB and LAMP2 in WT and PLD3$^{-/-}$ cells with or without synthetic Aβ$_{1-42}$ incubation. Bars are mean ± S.E.M., *n=7*. $^{*}p < 0.05$ by one-way ANOVA followed by Tukey's multiple comparisons test.

872 D) Western blot analysis of CTSB in the superior temporal lobe protein fraction. Each lane
873 corresponds to a donor of the indicated group. Data presented mean ± S.E.M., non-AD *(n=11),*
874 and AD brains *(n=16)*. $^{*}p < 0.05$ and $^{**}p < 0.01$ by Welch's unequal variances *t*-test.
875 F) Representative confocal microscopy images of CTSB-LAMP2 colocalization in non-AD and
876 AD sections. Data presented are means (Pearson's correlation coefficient, PCC, (r)) ± S.E.M.,
877 *n=7*, each with five images $^{*}p < 0.05$ by unpaired *t*-test. The scale bars are 5 μm.
878 G) CTSB in the cerebral vasculature. Representative confocal microscopy images and
879 quantification of CTSB expression pattern *(green)* in the temporal lobe from non-AD and AD
880 cases. Mean CTSB intensity in vascular regions was quantified solely in the collagen-IV
881 immunoreactive area *(red)*. β-amyloid aggregates and cerebrovascular amyloid deposition were
882 detected with MX04 *(blue)* and microglia by the marker Iba1*(grey)*. Data presented mean ±
883 S.E.M., *n=9*, each with at least five images. $*p < 0.05$ by unpaired *t*-test. The scale bars are 50
884 μm.
885 H) Western blot analysis of the level of CTSB in isolated human vessels from the temporal lobe
886 protein fraction from non-AD and AD cases. Bars are mean ± S.E.M., *n=5*. $*p < 0.05$ by
887 unpaired *t*-test.
888
889

Figure 4. PLD3 regulates TFEB/TFE3 metabolism. The proteasome, rather than lysosomes, is predominantly involved in PLD3-mediated TFEB/TFE3 metabolism.

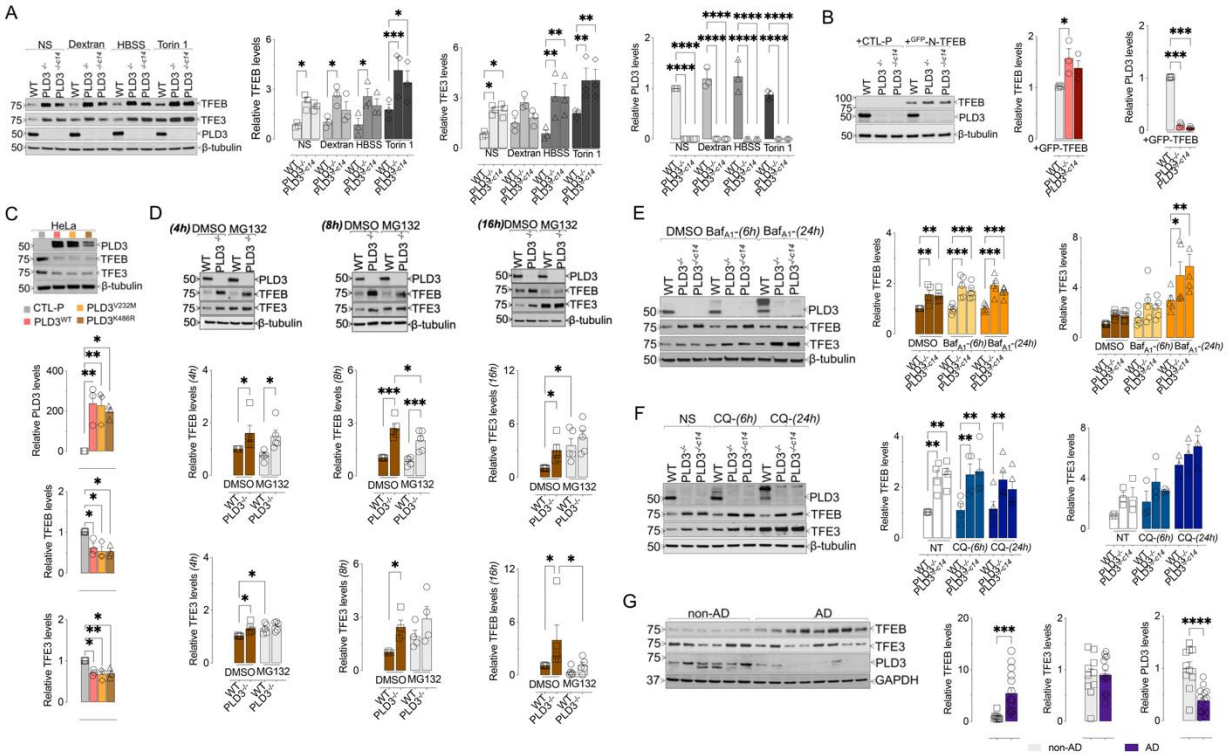

A) Western blot analysis of TFEB, TFE3, and PLD3 in WT and PLD3$^{-/-}$ cells treated with vehicle (NS, *non-stimulation*), dextran (0.25 mg/mL), HBSS, or Torin 1 (1 mM) for 3 hours. Proteins were quantified, expressed compared to β-tubulin, compared between genotypes, and presented as mean ± S.E.M., *n=3*. $^{*}p < 0.05$, $^{**}p < 0.01$, and $^{****}p < 0.0001$ by two-way ANOVA followed by uncorrected Fisher's LSD.

B) Western blot analysis of TFEB and PLD3 in WT and PLD3$^{-/-}$ cells transfected with control plasmids (CTL-P) or GFP-tagged TFEB plasmids (GFP-N-TFEB) for 2 days. TFEB and PLD3 were quantified relative to β-tubulin and compared between genotypes (mean ± S.E.M., *n=3*). $^{*}p < 0.05$, and $^{****}p < 0.0001$ by two-way ANOVA followed by uncorrected Fisher's LSD.

902 C) Western blot analysis of TFEB, TFE3, and PLD3 in HeLa cells transfected with control
903 plasmids (CTL-P) or PLD3 plasmids for 2 days. Proteins were quantified relative to β-tubulin
904 and compared between genotypes (mean ± S.E.M., *n=3*). $^{*}p < 0.05$, and $^{**}p < 0.01$ by one-way
905 ANOVA followed by Dunnett's multiple comparison test.
906 D) Western blot analysis of TFEB, TFE3, and PLD3 in WT and PLD3$^{-/-}$ cells treated with
907 MG132 (1 mM) for 4, 8, and 16 hours. Proteins were quantified relative to β-tubulin and
908 compared among experimental conditions (mean ± S.E.M., *n=4-5*). $^{*}p < 0.05$, $^{***}p < 0.001$ by
909 two-way ANOVA followed by uncorrected Fisher's LSD.
910 E and F) Western blot analysis of TFEB, TFE3, and PLD3 in WT and PLD3$^{-/-}$ cells treated with
911 (E) bafilomycin A1 (BafA1, 200 nM, *n=5*) or (F) chloroquine (CQ, 50 mM, *n=4*) for 6 hours
912 and 24 hours. Proteins were quantified relative to β-tubulin and compared among experimental
913 conditions (mean ± S.E.M). $^{*}p < 0.05$, $^{**}p < 0.01$, and $^{***}p < 0.001$ by two-way ANOVA
914 followed by uncorrected Fisher's LSD.
915 G) Representative western blot analysis of TFEB, TFE3, and PLD3 levels in superior temporal
916 lobe protein lysate from human brain. Each lane corresponds to a donor of the indicated group.
917 Data are normalized to GADPH (means ± S.E.M., non-AD *n=10*, and AD *n=15*). ***$p < 0.001$
918 by Welch's unequal variances *t*-test.
919
920

Figure 5. Loss of PLD3 augments TFEB/TFE3 transcription and nuclear localization.

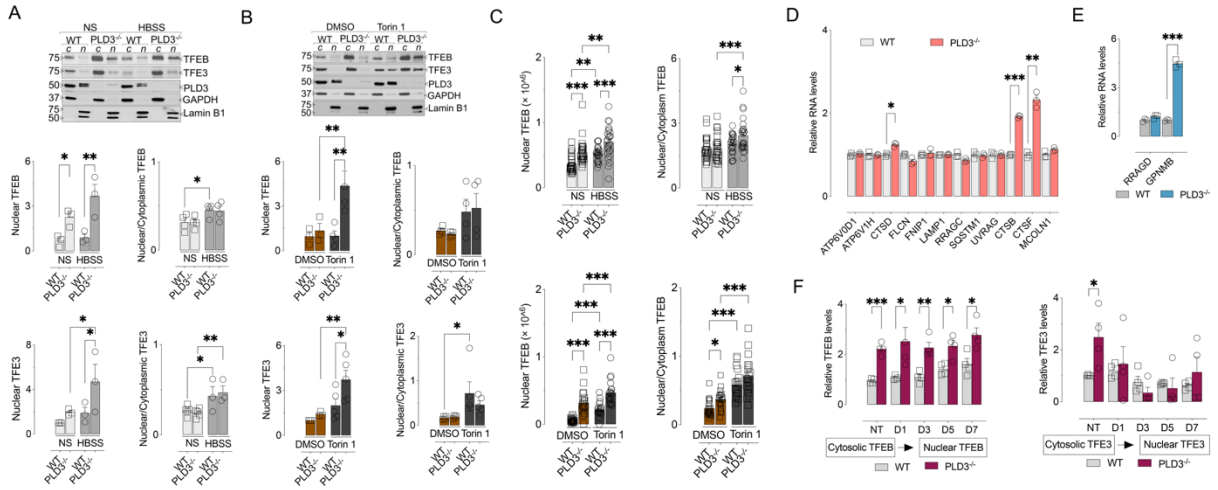

A and B) Western blot analysis of TFEB, TFE3, and PLD3 in nuclear extract *(n)* and cytoplasmic extract *(c)* of WT and PLD3$^{-/-}$ cells treated with (A) HBSS (*vs.* NS *(non-stimulation)*), or (B) 1 μM Torin 1 (*vs.* DMSO) for 3 hours. Proteins were quantified and normalized to GAPDH *(cytoplasmic)* or Lamin B1 *(nuclear)*. Proteins in *n* or their *n*-to-*c* ratios were compared among experimental conditions and presented as mean ± S.E.M., *n=3-5*. $^{*}p < 0.05$ and $^{**}p < 0.01$ by two-way ANOVA followed by uncorrected Fisher's LSD.

C) Immunostaining analysis of TFEB location in WT and PLD3$^{-/-}$ cells treated with HBSS (*vs.* NS *(non-stimulation)*) or 1 μM Torin 1 (*vs.* DMSO) for 3 hours. Data presented means ± S.E.M., *n=20-25* fields. $^{*}p < 0.05$, $^{**}p < 0.01$, and $^{***}p < 0.001$ by two-way ANOVA followed by uncorrected Fisher's LSD.

D and E) Transcript levels of genes containing the CLEAR motif (D) or genes responsive to TFEB (E) in WT and PLD3$^{-/-}$ cells were calculated and compared between WT and PLD3$^{-/-}$. Data presented means ± S.E.M., *n=3*. $^{*}p < 0.05$, $^{**}p < 0.01$, and $^{***}p < 0.001$ by multiple unpaired *t*-tests.

937 F) Outcome of long-term incubation with synthetic $A\beta_{1-42}$ on TFEB and TFE3 location. Proteins

938 were quantified relative to β-tubulin and compared among experimental conditions (mean ±

939 S.E.M., *n=4*). $^{*}p < 0.05$, $^{**}p < 0.01$, and $^{***}p < 0.001$ by two-way ANOVA followed by Fisher's

940 LSD multiple comparison test.

941